Available online at www.sciencedirect.com
SCIENCE DIRECT®
Journal of Molecular Catalysis A: Chemical 239 (2005) 41–48
JOURNAL OF MOLECULAR CATALYSIS A: CHEMICAL
www.elsevier.com/locate/molcata

The influence of impregnating pH on the postnatal and steam reforming characteristics of a Co-Ni/Al_2O_3 catalyst

Kelfin M. Hardiman, Cheng-Han Hsu, Tan T. Ying, Adesoji A. Adesina *

Reactor Engineering and Technology Group, School of Chemical Engineering and Industrial Chemistry, University of New South Wales, Anzac Parade, Sydney, NSW 2052, Australia

Received 22 March 2005; received in revised form 13 May 2005; accepted 16 May 2005
Available online 6 July 2005

Abstract

Bimetallic alumina supported Co-Ni catalysts were prepared by impregnation under low (2) and high (8) pH values. Support dissolution due to acid attack appeared to be responsible for the low BET surface area for catalyst obtained at pH 2. However, this low-pH catalyst possesses higher dispersion and superior metal surface area. This is ascribed to the charged-induced migration of metal cations towards the grain centre where adsorption sites are located as a result of the formation of positively charged alumina surface at low pH. Ammonia NH_3-TPD analysis showed that the surface of both catalysts was populated with weak Lewis acid sites though a higher site concentration was found on the high-pH catalyst. TEM images further revealed an eggyolk profile for the catalyst impregnated at pH 2 with metal species located in the particle interior; while in the catalyst synthesised at pH 8, the impregnant metal is concentrated around the external surface of the particle. XRD analysis of the catalysts before and after reduction indicates that the basic catalyst was more difficult to reduce probably because of higher metal aluminate content. This was further confirmed by the lower degree of reduction shown for this catalyst during the thermogravimetric TPR–TPO runs. Solid-state kinetic data of the catalyst calcination, reduction and oxidation conformed with the Avrami–Erofeev model. In particular, the ratios of the associated kinetic rate constants for calcination and oxidation parallel those obtained for the deactivation and steam reforming constants, respectively, in both catalysts. Thus, it may be possible to have an a priori knowledge of the comparative reaction and deactivation behaviour of different catalysts from the temperature-programmed kinetics of their nascent solid states.

Keywords: Bimetallic Co-Ni; Impregnation pH; Catalyst characterisation; Thermogravimetric analysis (TGA); Steam reforming of propane

1. Introduction

Although the formation of metallic phases possessing active sites is primarily determined by calcination variables, the amount of metal ions adsorbed and depth of penetration into the support pores are controlled during impregnation [1]. As impregnation pH level drops below the isoelectric point (ISP) of the support material, the surface charge becomes predominantly positive and vice versa. The mobility and deposition of these ions to form dispersed phase on the surface are therefore largely influenced by solution acidity.

The importance of optimum impregnation profiles is particularly critical to the design of steam reforming catalysts. To be sure, for industrial applications where operational conditions would permit mass transfer dominance, it is desirable to have impregnation carried out so that the catalytic ingredients are deposited as close as possible to the exterior of the catalyst pellet. On the other hand, for kinetically controlled reaction, uniform distribution profile of the impregnated catalyst is required [2].

Santacesaria et al. [3] indicated aluminium dissolution arising from chemical attack is responsible for the creation of adsorption sites. Displaced aluminium may also be re-adsorbed along with the metal ions onto the surface. This mixed adsorption process further enhances the metal adsorption rate, but may contribute to formation of metal aluminates

* Corresponding author. Tel.: +61 2 9385 5268; fax: +61 2 9385 5966.
E-mail address: a.adesina@unsw.edu.au (A.A. Adesina).

1381-1169/$ – see front matter © 2005 Elsevier B.V. All rights reserved.
doi:10.1016/j.molcata.2005.05.030

at the oxide surface [4]. According to Olsbye et al. [5], reactions at the solid–liquid interface due to pH change can be described by:

(i) Protonation of the surface

$$\text{Al–OH} + \text{H}^+ \leftrightarrow \text{Al–OH}_2{}^+ \text{ at low pH} \quad (1)$$

$$\text{Al–OH} + \text{OH}^- \leftrightarrow \text{Al–O}^- + \text{H}_2\text{O} \text{ at high pH} \quad (2)$$

(ii) Dissolution of alumina

$$\text{Al}_2\text{O}_3 + 6\text{H}^+ \leftrightarrow 2\text{Al}^{3+} + 3\text{H}_2\text{O} \text{ at low pH} \quad (3)$$

$$\text{Al}_2\text{O}_3 + 2\text{OH}^- + 3\text{H}_2\text{O} \leftrightarrow 2\text{Al(OH)}_4{}^- \text{ at high pH} \quad (4)$$

In our previous work [6], Co-Ni/Al_2O_3 prepared by wet impregnation had been successfully employed to effect steam reforming under low steam-to-carbon (S:C) feed condition (S:C < 2). In this study, we examined the role of pH of the impregnating solution on the physicochemical attributes of the catalyst, its steam reforming activity as well as resilience to deactivation under conditions, which deliberately favoured modest carbon deposition. We therefore considered two limiting pH values of 2 and 8 since causticisation of the alumina proceeds rapidly at pH > 10.

2. Experimental details

For the catalyst preparation, alumina (Norton, USA) extrudates were initially crushed to sizes of 180–250 μm and pre-treated in a furnace at 1073 K for 6 h. This thermal treatment was carried out to ensure morphological stability during subsequent application. One hundred grams of the pre-treated alumina was then charged into a 500 ml beaker filled with approximately 250 ml of deionised water. Calculated amount of cobalt nitrate (Sigma–Aldrich, USA) was added into the slurry and kept at 303 K by a hot-plate. pH was adjusted and maintained throughout the 3 h stirring process using either 3.0 M HNO_3 (for pH 2) or 6.0 M NH_4OH (for pH 8). The pH level and temperature were monitored using a TPS Benchtop pH meter equipped with a temperature probe. The slurry was dried for 12 h in an oven at 393 K. The dried solid was further impregnated with nickel nitrate (May & Baker, England) solution to yield desired Ni loading following a similar procedure and drying protocol. The resulting solid was calcined at 973 K for 5 h at 5 K min^{-1} in air supplied at 200 ml min^{-1}. Finally, the calcined solid was crushed and sieved to 212–250 μm.

Various characterisation techniques were used to secure the intrinsic properties of the prepared catalysts. A Micromeritics Autochem 2910 unit was used to measure BET surface areas by nitrogen adsorption at 77 K. H_2 chemisorption and NH_3-TPD experiments were also carried out using the same instrument to measure dispersion, metallic surface area and particle size as well as NH_3 heat of desorption and acid strength, respectively. H_2 uptake was performed at 373 K following outgassing with the He at 873 K for 2 h. The ammonia TPD runs also involved sample outgassing at 573 K for 30 min in helium flow, followed by adsorption using 0.4% NH_3/He for 1 h at 423 K. The desorbed ammonia concentration was monitored by a thermal conductivity detector during heating in helium flow to 973 K at various heating rates of 10, 15, 20 and 25 K min^{-1}. Microscopic images were also obtained by transmission electron microscopy (TEM) using Hitachi H-7000, while XRD measurement was recorded on a Philips X'pert system using Ni-filtered Cu Kα (λ = 1.542 Å) at 40 kV and 30 mA. Thermogravimetric runs were conducted on a ThermoCahn TG-2121 TGA unit. Approximately 0.1 g of uncalcined specimen was initially loaded into the sample boat. The calcination experiment was performed using high-purity air at 55 ml min^{-1}. Double-cycle reduction–oxidation (TPR–TPO–TPR–TPO) runs were also carried out with the same instrument to investigate reducibility and re-oxidation characteristics of the oxide phases present after calcination. The temperature-programmed run was always preceded with inert gas (N_2) treatment at 423 K for 1 h to remove moisture and other possible impurities. During the cycle, all gas flows were maintained at 55 ml min^{-1} using composition of 50% H_2/N_2 for TPR and high-purity air for TPO. Heating was performed at 5 K min^{-1} to 973 K and maintained there for 1 h.

Activity tests were performed in a fluidised bed system. The detailed rig set-up and operating conditions have been described in an earlier publication [7]. The reactor typically contained 1 g of catalyst and reduced in pure hydrogen (200 ml min^{-1} NTP) at 873 K for 2 h. The reforming reaction was carried out using propane as hydrocarbon substrate for 6 h at 773 K. Inert helium gas was used as diluent to maintain constant total gas flow to the reactor at 400 ml min^{-1}. Coking resilience of these catalysts was assessed under the stoichiometric feed ratio (i.e. S:C = 1) since conventional steam reforming runs required S:C > 2 to avoid coking. The product stream was analysed using a Shimadzu TCD gas chromatograph (model 8A). Carbon content in the spent catalysts was then determined using a Shimadzu Solid Sample Module SSM-5000A coupled to Total Organic Carbon (TOC) Analyzer 5000A.

3. Results and discussion

3.1. Catalyst characterisation

The two types of catalysts were characterised using liquid N_2 adsorption at 77 K, H_2 chemisorption and temperature-programmed NH_3 desorption to obtain surface area, pore volume, metal dispersion and particle diameter as well as surface acidity and strength since these innate physiochemical attributes have a bearing on catalyst performance. As may be seen from Table 1, the acid catalyst (Catalyst A) has signif-

Table 1
Physicochemical properties

Catalyst	A (pH 2)	B (pH 8)
BET ($m^2\,g^{-1}$)	108.62	162.33
Pore volume ($ml\,g^{-1}$)	0.444	0.702
Pore diameter (A)	128.97	154.72
Dispersion (%)	5.62	3.87
Metal surface area ($m^2\,g^{-1}$)	7.52	5.17
Metal particle diameter (nm)	17.94	26.07
Heat of desorption ($kJ\,mol^{-1}\,K^{-1}$)	40.19	41.33
NH_3 desorbed ($\mu mol\,g^{-1}$)	1.409	1.555

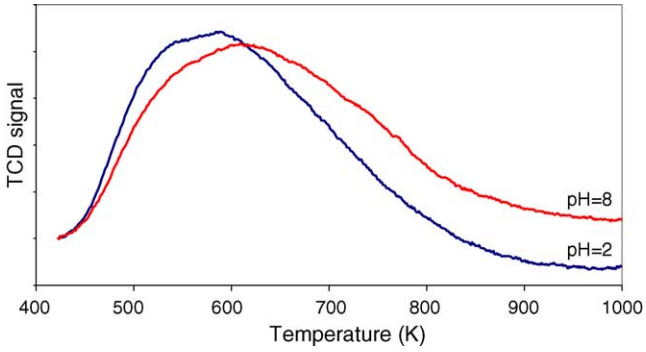

Fig. 1. NH_3-TPD spectra.

icantly lower surface area and pore volume ($108.62\,m^2\,g^{-1}$ and $0.444\,ml\,g^{-1}$, respectively) than Catalyst B (prepared at pH 8). This change in textural properties may be due to pore blockage of the alumina support pores by relatively large metal particles or an indication of bulk phase morphological modification as a result of acid or base attack during metal impregnation. As H_2 uptake measurements later revealed, the crystallite size in Catalyst A was smaller than that produced on Catalyst B and it would therefore seem that the lower surface area and pore volume obtained in low-pH catalyst is attributable to structural changes in the alumina support during the metal impregnation. We posit that alumina dissociation arising from acid attack at pH 2 was responsible for the decrease in total surface area and pore volume during catalyst preparation as suggested by Eq. (3). On the other hand, caustication of the alumina support via Eq. (4) was negligible at pH 8 due to the nearly equilibrated charge transfer between the alumina surface and the surrounding solution since the isoelectric point (IEP) of alumina is reportedly located at pH 8.2 based on electrophoretic study of γ-alumina suspensions by Heise and Schwarz [1]. It is noteworthy that the BET area and pore volume of pure γ-alumina reported as $181\,m^2\,g^{-1}$ and $0.808\,ml\,g^{-1}$, respectively [8] are closer to those of the high-pH catalyst.

H_2 chemisorption data at 373 K revealed that the metal dispersion on the acid catalyst was higher (5.62%) than on Catalyst B (3.87%) with associated metal particle size 17.94 and 26.07 nm, respectively. The superior metal dispersion in Catalyst A may be due to better mobility and deeper penetration of the aqueous metal nitrate ions into the porous alumina support at low pH. Indeed, studies by Chen et al. [4] and Mieth and Schwarz [9] using nickel salt in alumina matrix also lend credence to this interpretation.

The type and strength of acid site(s) on the catalyst are also influenced by the pH of the impregnating solution. NH_3-TPD spectra for both catalysts shown in Fig. 1 revealed a single broad peak located at 590 K (for Catalyst A) and 600 K (for Catalyst B). Desorption peak temperature, T_D, greater than 673 K is symptomatic of a strong acid site [10] while the value of the heat of desorption, $-\Delta H_D$, helps to determine the type of acid site. Bronsted acid sites are generally characterised by $-\Delta H_D$ in the range 125–145 $kJ\,mol^{-1}$ [11] while Lewis sites possess much lower $-\Delta H_D$-value. The location of the desorption peaks below 673 K suggests that the surface of both catalysts is primarily populated by weak Lewis acid sites. This qualitative inference is supported by the nearly identical NH_3 heat of desorption (40–41 $kJ\,mol^{-1}$) estimated for the catalysts as seen in Table 1. Even so, the modest difference in amount of NH_3 desorbed (ca. 0.15 $\mu mol\,g^{-1}$) is a reflection of the higher concentration of oxide species present in Catalyst B. It is well known that in multicomponent oxide systems, the interface between two different metal oxides represents centres of significant acidity. In the present catalyst formulation, it appears that nearly identical types of oxides (NiO, Co_3O_4, $NiCo_2O_4$, $CoAl_2O_4$ and/or $NiAl_2O_4$) were formed under both high and low pH albeit with different concentrations.

Additional information from TEM images (cf. Fig. 2) of the reduced catalysts also show that the metal species were located further inside the particle centre in Catalyst A – a phenomenon commonly referred to as eggyolk profile – while in Catalyst B, the metal appeared to be deposited closer to the particle exterior. This observation has also been seen for a similar catalyst prepared by Geus and van Veen [12]. Scanning electron micrographs of the catalyst specimens exhibited in Fig. 3 also confirmed the smaller particle size and finer metal dispersion associated with Catalyst A.

In Fig. 4 are plotted the X-ray diffractograms of the two catalysts before and after reduction. In the unreduced state, both catalysts revealed strong peak intensities for $CoAl_2O_4$ ($2\theta = 36.7°$) and $NiAl_2O_4$ (37° and 44.8°). Modest amounts of spinel-type $NiCo_2O_4$ (31° and 36.6°), Co_3O_4 (31.2° and 36.8°) and NiO (43.2°) are also apparent. Consistent with NH_3-TPD data, the basic catalyst contained higher concentration of the metal aluminate ($CoAl_2O_4$ and $NiAl_2O_4$). Comparison of the XRD spectra between the oxide and reduced catalysts shows that upon reduction, the $NiCo_2O_4$, Co_3O_4 and NiO phases were totally converted to metallic phases Co (44.2° and 51.5°) and Ni (44.5° and 51.8°). There was also a significant decrease in the peak intensity for the metal aluminates ($2\theta = 37°$). Further inspection reveals that the extent of reduction was higher in Catalyst A than Catalyst B. This is consistent with previous chemisorption analysis, which gave higher H_2 uptake and hence percent metal dispersion and metal surface area in the acid catalyst than the basic catalyst.

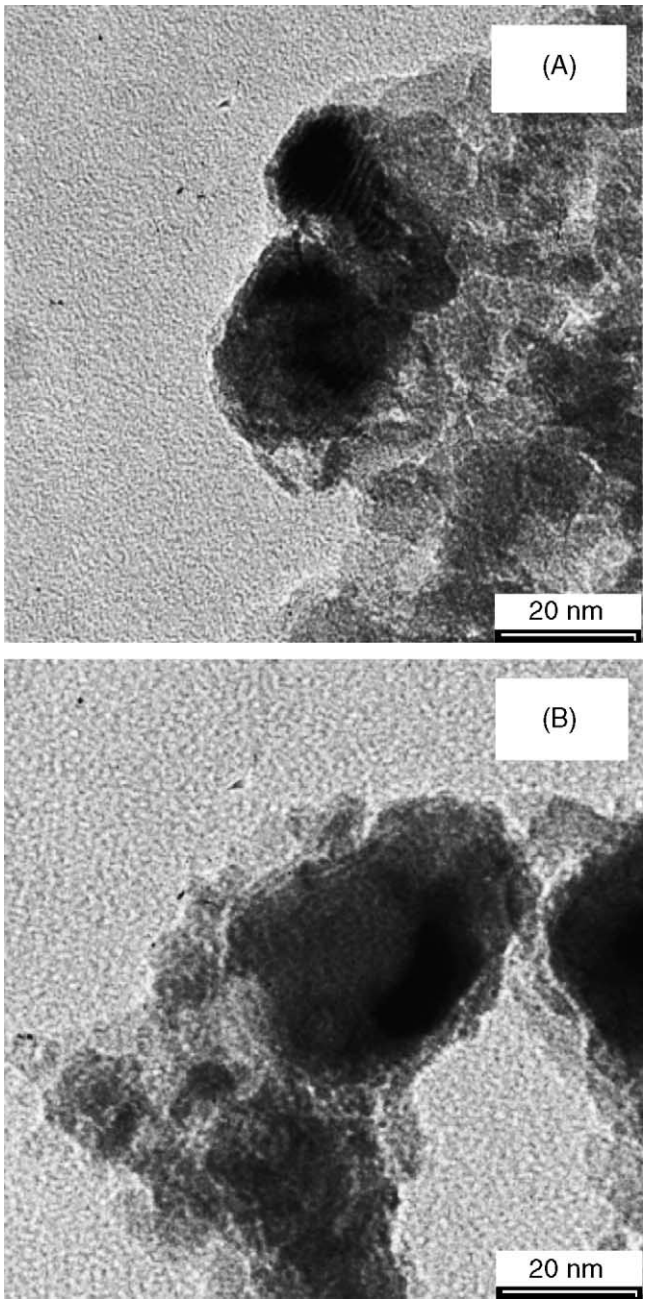

Fig. 2. TEM micrographs for reduced Catalysts A (pH 2) and B (pH 8).

3.2. Thermogravimetric fingerprinting

The thermal characteristics of the solid catalysts were examined with temperature-programmed calcination, reduction and oxidation. Analysis of the solid-state reaction kinetics provides information on the stability of the various oxide and reduced phases present in each catalyst and are therefore related to their performance under steam reforming conditions.

Fig. 5 shows the complete thermal cycle (double TPR–TPO sequence) for both catalysts. The weight derivative–temperature profiles shown in Fig. 6 highlight important fingerprints of the solid phases during each stage of the thermal treatment for the two catalyst types. It is evident that from curves (a and b) that the main metal nitrate decomposition during calcination took place about 492 K to yield metal oxides (NiO, $NiCo_2O_4$ and Co_3O_4). A second, although relatively small shoulder observed at the higher temperature (520 K), is indicative of the decomposition of the aluminium nitrate back to the alumina since nitric acid attack occurs to some extent during wet chemistry. Consequently, this shoulder is somewhat more prominent at pH 2. Beyond these decomposition temperatures, the oxide catalysts remained practically stable up to 973 K. The rather sharp and narrow peak for the basic catalyst suggests that the nitrate decomposition rate was higher than in Catalyst A (which has a broader and shorter peak). The H_2 reduction spectra for the two catalysts depicted by curves (c and d) exhibit multiple peaks at 493, 655 and 968 K. The lowest temperature peak represents the reduction of Ni_2O_3 (a small XRD-amorphous species) [6], while the large broader peak at about 655 K is assigned to the dominant metal oxide phase containing mainly NiO, Co_3O_4, $NiCo_2O_4$ and the highest temperature peak at 968 K is due to the reduction of the metal aluminate phase. It is interesting that upon re-oxidation (profiles (e and f)) in air, the catalyst was restored to the initial oxidation state produced from direct calcination of the parent nitrate as evidenced by a single large peak at about 495 K. During the second temperature-programmed H_2 reduction, the presence of small quantities of Ni_2O_3 (shoulder at 493 K) and a larger broader peak at 716 K assigned to the reduction of the major metal oxides is clearly seen in curves (g and h). The right shift of this peak from 655 (in the first reduction cycle) to 716 K (in the second reduction cycle) is a reflection of the change in composition of the constituent metal oxides upon re-oxidation of the Co^0 and Ni^0 species back to NiO, Co_3O_4, CoO and $NiCo_2O_4$ in curves (e and f). The slight hump at 973 K in both (g and h) suggests additional reduction of the metal aluminate phase left over from the first reduction TPR I. In the final stage of the thermal treatment, catalysts were again re-oxidised (TPO II). The spectra represented by curves (i and j) practically mirrored the behaviour in (e and f) suggesting reproducibility of the same composite oxide phase. There is, however, a right-shift in peak temperature to about 540 K (from the previous 495 K for (e and f)) probably due to the variation in the metal oxide composition.

Table 2 displays the percent weight change at each stage of the thermal treatment and the corresponding extent of conversion (in parenthesis). It is apparent that Catalyst A is generally easier to reduce and oxidise than Catalyst B in the double-cycle TPR–TPO although both were essentially fully decomposed during the calcination stage. Since steam reforming conditions present a variable mixture of reducing and oxidising conditions, it seems that Catalyst A would yield a more stable performance in the long term especially, since the extent of conversion in both reducing and re-oxidising conditions are almost identical as seen between TPR II (70.2%) and TPO II (69.6%) in Table 2.

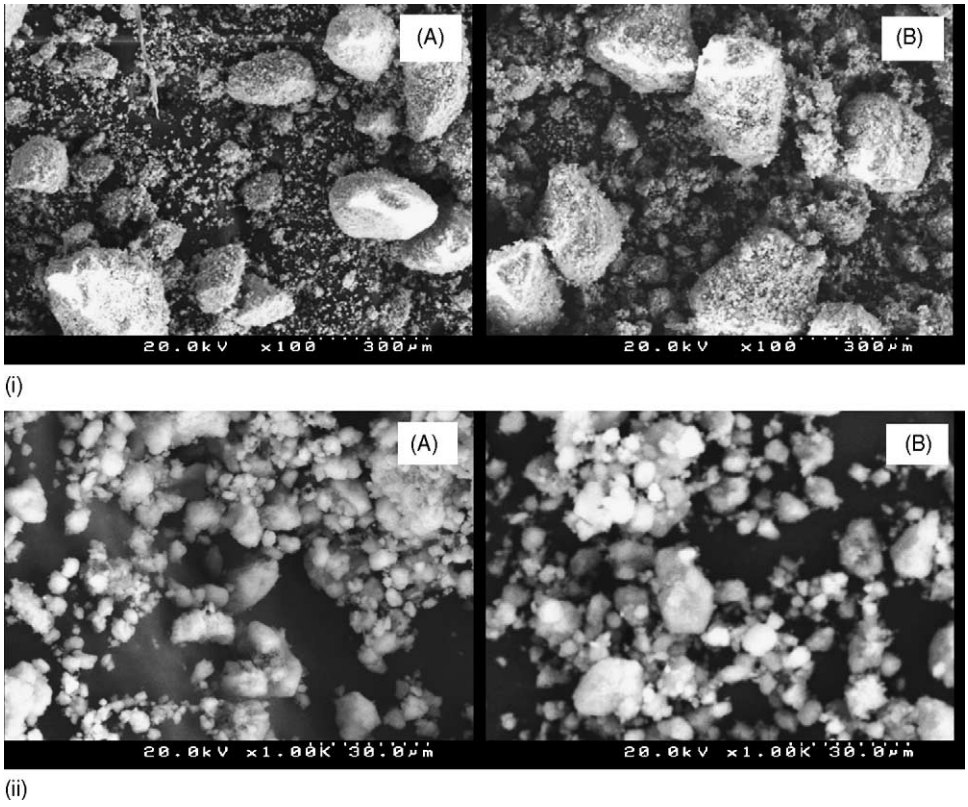

Fig. 3. SEM images for reduced Catalysts A (pH 2) and B (pH 8) under: (i) 100× magnification and (ii) 1000× magnification.

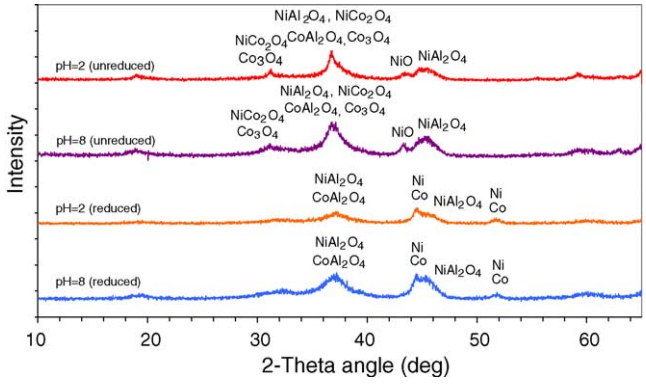

Fig. 4. XRD diffractograms of unreduced and reduced catalysts.

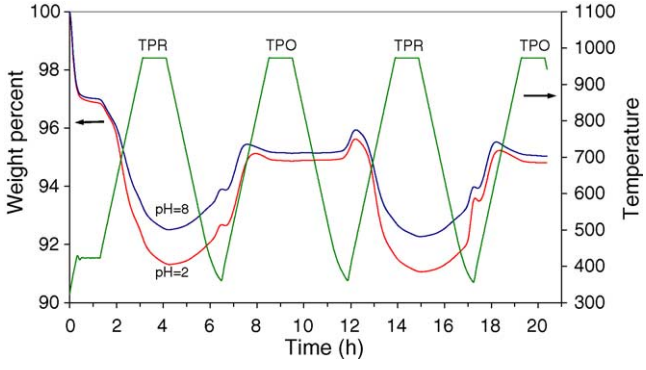

Fig. 5. Weight profiles of TPR–TPO–TPR–TPO runs.

Based on the thermogravimetric analysis (TGA) profiles, the transient solid conversion, α, during each solid-state reaction was obtained from:

$$\alpha = \frac{w_i - w}{w_i - w_f} \tag{5}$$

where w is the instantaneous weight, w_i the initial weight and w_f is the final weight. The α–t profiles (not shown) have the characteristic sigmoid shape indicating that the kinetic data may be analysed in terms of the reaction-rate controlling Avrami–Erofeev (A–E) model [13]. The associated reaction rate constant, k_s, for each stage (calcination, reduction and oxidation) of the TGA cycle, may be obtained from the nth order Avrami–Erofeev model given by,

$$-\ln[(1-\alpha)]^{1/n} = k_s t, \quad 2 \le n \le 4 \tag{6}$$

Table 2
Percent weight changes and extents of conversion for calcination and TPR–TPO–TPR–TPO runs

	Percent of weight change (%)	
	A (pH 2)	B (pH 8)
Calcination	29.154 (0.983)	35.028 (1.000)
TPR I	5.690 (1.000)	4.590 (0.824)
TPO I	3.649 (0.655)	2.700 (0.485)
TPR II	3.911 (0.702)	2.947 (0.529)
TPO II	3.874 (0.696)	2.857 (0.513)

The values in parenthesis indicate the extent of conversion.

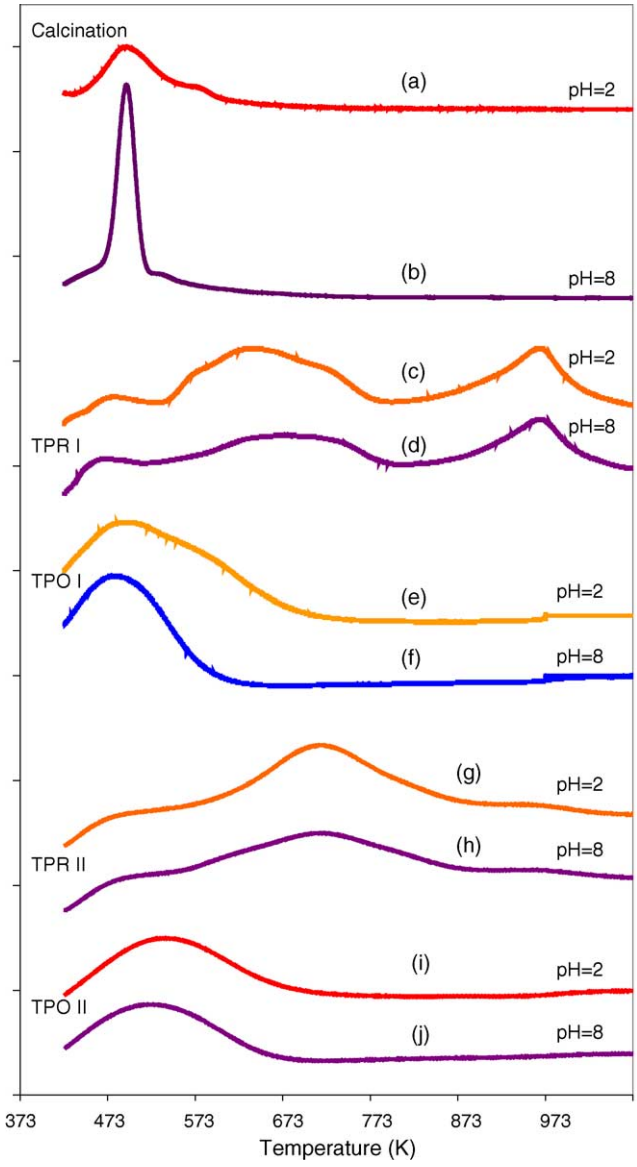

Fig. 6. Calcination and TPR–TPO–TPR–TPO weight derivative profiles.

where t is time in hours. Table 3 hosts the k_s-values for the various Avrami–Erofeev models ($n = 2$, 3 and 4) considered. The numbers in parenthesis are the relevant R^2-coefficients of the model. Due to the relatively small size of the lowest temperature H_2-TPR peak assigned to the Ni_2O_3 species, the corresponding data were not fitted to Avrami–Erofeev models; hence, Peaks 1 and 2 in the TPR stages belong to the metal oxide phase (Peak 1) and the metal–support interaction metal aluminate phase (Peak 2). In general, the qualitative trend across row between the two Catalysts A and B is similar suggesting that the kinetic implications of the data are not model-dependent. Although it appears that any of the three Avrami–Erofeev models may be used to reasonably represent the solid-state reaction rate data, estimates from $n = 3$ seemed to be the most preferable (based on R^2-values). In agreement with the previous inference from the calcination

Table 3
Kinetic coefficients (h^{-1}) and R^2-values using Avrami–Erofeev (A–E) model for calcination, TPR and TPO

n in the A–E model	Calcination		TPR I				TPO I		TPR II				TPO II	
	A	B	1		2		A	B	1		2		A	B
			A	B	A	B			A	B	A	B		
2	6.306 (0.969)	15.590 (0.423)	2.489 (0.961)	2.736 (0.952)	3.840 (0.952)	4.112 (0.920)	2.309 (0.971)	4.402 (0.958)	2.200 (0.973)	2.239 (0.965)	–	–	4.021 (0.945)	5.440 (0.935)
3	4.446 (0.985)	12.222 (0.508)	1.756 (0.983)	1.944 (0.977)	2.727 (0.982)	2.916 (0.927)	1.607 (0.990)	3.132 (0.982)	1.566 (0.990)	1.594 (0.983)	–	–	2.233 (0.966)	3.075 (0.950)
4	3.471 (0.981)	10.209 (0.520)	1.374 (0.980)	1.524 (0.977)	2.139 (0.985)	2.285 (0.905)	1.256 (0.984)	2.459 (0.945)	1.234 (0.981)	1.256 (0.974)	–	–	1.532 (0.975)	2.126 (0.957)

The numbers in parenthesis are the R^2-coefficients.

thermal spectra, the k_s-value for Catalyst B is more than twice its value for Catalyst A regardless of the kinetic model considered. However, the H_2 reduction rate constant during TPR is smaller than the nitrate decomposition rate constant. For Catalyst A, the ratio of the TPR kinetic constant to that of the calcination ($k_{s,TPR}/k_{s,cal}$) for Peak 1 (the oxide phase) is about 0.40 while the corresponding ratio for the B-type is about 0.16. This would suggest that the acid catalyst was easier to reduce than the basic catalyst, although the actual kinetic constants for the two types of catalyst are nearly the same for each Avrami–Erofeev model. As earlier signalled by XRD spectra, the metal aluminate phase (Peak 2) was also partially reduced, the ratio of the k_s-value for both catalysts is essentially unity (1.07) irrespective of the model used, corroborating the fact that the same species ($NiAl_2O_4$ and $CoAl_2O_4$) were reduced in both catalysts as XRD data have indicated. These kinetic constants were higher than the corresponding estimates for Peak 1 since they were obtained from conversion data at higher temperature (973 K). By comparison, the k_s-values for calcination step obtained at about 493 K were higher than those for the H_2 reduction (at 655 K) because of the different chemistries involved. Subsequent re-oxidation (TPO I) showed that the reduced catalysts may be reinstated to the original oxidation state as may be inferred from the re-appearance of the TPO peak at about 495 K. However, the k_s-values for both catalysts were now much smaller (<40%) than those obtained for oxide produced from nitrate decomposition. This again suggests that the observed rate constant k_s is not a simple first-order parameter depending only on temperature but also a function of the solid history. This is a testament to the complex mechanisms involved in solid-state reactions making direct application of concepts in homogenous reaction fraught with dangers. Indeed, the S-shaped conversion–time profiles observed during the thermal treatment of the catalysts here suggest that the solid-state reactions (for each stage) indicate that multiple steps, such as formation and growth of nuclei, agglomeration, dislocation and point defects, are involved in the solid transformation process. The second TPR revealed only a single peak (716 K) and here again, the k_s-values are nearly identical for both types of catalysts confirming that similar oxide phases were being reduced. In particular, these estimates are only marginally different from those for the first TPR profile. Kinetic analysis of the second TPO run also provided the k_s estimates in the last two columns of Table 3. Although these values are somewhat bigger than the corresponding values for TPO I, the qualitative similarity is obvious.

3.3. Steam reforming performance

Fig. 7 shows the time-on-stream behaviour of the two catalysts under steam reforming conditions at a steam-to-carbon (S:C) ratio = 1, which permits simultaneous carbon deposition. It is clear from these transient conversion data that although Catalyst B exhibited a higher average conversion within the first 3 h, it lacked stability in the long term.

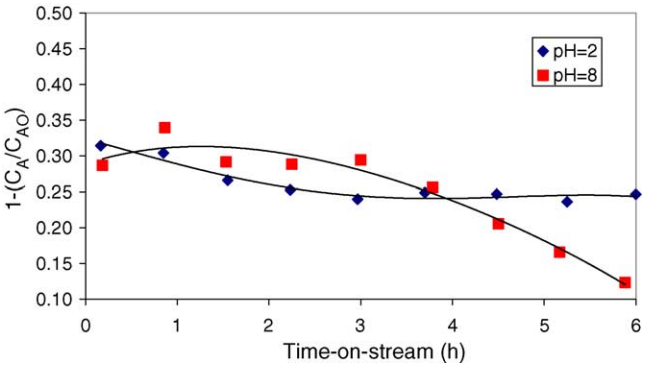

Fig. 7. Propane conversion profiles.

However, Catalyst A with an initially lower conversion settled down to a constant conversion after about 2 h on-stream at a level higher, after this period, than Catalyst B.

From these data, it is possible to extract the steam reforming constant, k', and the deactivation coefficient, k_d, using an appropriate reaction-deactivation model from the generalised expressions derived in our previous paper [14]. For a well-mixed reactor, such as a fluidised bed reformer, the pertinent model for propane reforming under low S:C ratio is:

$$\frac{1}{\left(\frac{C_{A_0}}{C_A} - 1\right)} = \frac{1}{k'\tau'} + \left(\frac{k_d}{k'\tau'}\right) t \tag{7}$$

where C_{A_0} and C_A are feed and instantaneous propane concentrations, respectively, while τ' is the reactor space-time. A fit of the data to this model yielded the estimates summarised in Table 4. Not surprisingly, Catalyst B has a higher (19.8) reaction velocity, k', than Catalyst A (10.3). However, the k_d-value for the basic catalyst is also bigger than in the acid catalyst. Since k' is a composite rate constant for both pure propane reforming and the associated dehydrogenation (to yield carbon), a lower value of k' for Catalyst A is also an indication of lower carbon deposition rates and hence, reduced deactivation rate, k_d. Even so, the carbon-resilience attribute of Catalyst A is seen from the higher k'/k_d ratio of about 157 compared to 34 for Catalyst B. Since TEM image of this catalyst revealed that metal deposition occurred primarily around the pore mouth, blockage due to carbon lay-down would be more severe as the metal sites for hydrocarbon adsorption would be more readily accessible than in Catalyst A with better metal dispersion. Indeed, the initially higher conversion on Catalyst B is consistent with this explanation since hydrocarbon conversion on the freshly reduced and more accessible

Table 4
Estimates of deactivation, k_d, and reforming, k', parameters

	Catalyst	
	A (pH 2)	B (pH 8)
k_d (s^{-1})	0.066	0.580
k' (L s^{-1} g cat.$^{-1}$)	10.3	19.8
k'/k_d (L g cat.$^{-1}$)	156.85	34.1

metal sites on the particle exterior have precedence over metal sites more uniformly distributed within the support interior (as in Catalyst A). However, as carbon build-up continues conversion would drop more quickly because of rapid loss of metal sites, whereas the more uniformly dispersed metal sites in Catalyst A would maintain a steadier conversion level due to relatively low carbon coverage. In particular, the larger crystallite size associated with Catalyst B presents a more suitable geometrical configuration for dehydropolycondensation of surface CH_x species to naphthalenic carbon polymers responsible for site blockage and loss in steam reforming activity. Thus, both in terms of location (distribution on the support) and metal particle size, Catalyst B has the greater propensity to carbon-induced deactivation.

Interestingly, post-mortem solid sample TOC analysis also confirmed that while Catalyst A has a carbon content of 44%, Catalyst B used under exactly the same S:C ratio possessed 56%. Furthermore, although both catalysts exhibited nearly identical solid H_2 reduction rate constants, since under steam reforming the catalyst tends to get oxidised, it is somewhat revealing that the ratio of the TPO oxidation rate constants ($k_{s,TPO,B}/k_{s,TPO,A}$) for both catalysts is approximately the same as the pseudo steam reforming constant, k'_B/k'_A (i.e. 2 and 1.8, respectively). Equally interesting, the ratio of the calcination rate constant between B and A—also parallels the deactivation rate coefficient ratio for the two catalysts. These trends in the ratio of identical reaction and deactivation constants for the two catalysts would suggest that it is possible to gain an a priori knowledge of catalyst performance under reaction conditions from the solid-state temperature-programmed kinetics of the nascent catalyst.

4. Conclusions

This study has shown that impregnating pH has a significant effect on the metal distribution within the catalyst support and consequently its physicochemical attributes, activity and deactivation. For the alumina-supported bimetallic catalyst investigated, acidic impregnation favoured better dispersion, metal surface area and superior reducibility. While the high pH-prepared catalyst gave an initially better steam reforming conversion, this was unsustainable because of severe carbon deposition on the metal sites, which are located on the particle exterior. However, Catalyst A prepared with a low pH (2) and a higher metal dispersion exhibited better long-term stability. The ratio of the propane steam reforming reaction rate constants for both catalysts was nearly identical to the solid-state kinetic constant obtained from TPO analysis. Similar trend was also observed for the calcination kinetic constant and the deactivation coefficient suggesting that the solid-state kinetic parameters from temperature-programmed treatment may signal the relative behaviour between different catalysts during actual reaction and eventual activity loss.

Acknowledgements

The financial support of this work by the Australian Research Council is gratefully acknowledged. KMH thanks the University of New South Wales for a University Postgraduate Award (UPA) while TTY is a recipient of the Singapore student exchange bursary. The authors are also indebted to Professors Eric Kennedy, Bodgan Dlugogorski and Dr. Hai Yu (University of Newcastle, Australia) for their kind assistance with the XRD runs.

References

[1] M.S. Heise, J.A. Schwarz, J. Colloid Interface Sci. 107 (1985) 237.
[2] A.A. Adesina, Appl. Catal. A 138 (1996) 345.
[3] E. Santacesaria, S. Carra, I. Adami, Ind. Eng. Chem. Prod. Res. Dev. 16 (1977) 41.
[4] S.L. Chen, H.L. Zhang, J. Hu, C. Contescu, J.A. Schwarz, Appl. Catal. 73 (1991) 289.
[5] U. Olsbye, R. Wendelbo, D. Akporiaye, Appl. Catal. A 152 (1997) 127.
[6] K.M. Hardiman, C.G. Cooper, A.A. Adesina, Ind. Eng. Chem. Res. 43 (2004) 6006.
[7] K.M. Hardiman, T.T. Ying, A.A. Adesina, E.M. Kennedy, B.Z. Dlugogorski, Chem. Eng. J. 102 (2004) 119.
[8] K. Opoku-Gyamfi, Ph.D. Thesis, University of New South Wales, 1999.
[9] J.A. Mieth, J.A. Schwarz, Appl. Catal. 55 (1989) 137.
[10] A. Auroux, R. Monaci, E. Rombi, V. Solinas, A. Sorrento, E. Santacesaria, Thermochim. Acta 379 (2001) 227.
[11] G. Yaluris, R.B. larson, J.M. Kobe, M.R. Gonzalez, K.B. Fogash, J.A. Dumesic, J. Catal. 158 (1996) 336.
[12] J.W. Geus, J.A.R. van Veen, in: R.A. van Santen, P.W.N.M. van Leewen, J.A. Moulijn, B.A. Averill (Eds.), Catalysis: An Integrated Approach, Elsevier, Amsterdam, 1999, pp. 459–484.
[13] M.E. Brown, Introduction to Thermal Analysis: Techniques and Applications, Kluwer Academic Publishers, The Netherlands, 2001, pp. 181–214.
[14] K.M. Hardiman, F.J. Trujillo, A.A. Adesina, Chem. Eng. Proc. 44 (2005) 987.